Chiral Helices Formation by Self-Assembled Molecules on Semiconductor Flexible Substrates

Hong Po, Corentin Dabard, Benoît Roman, Etienne Reyssat, Benoit Baptiste,
Emmanuel Lhuillier, Sandrine Ithurria

Chiral helices formation by self-assembled molecules on semiconductor flexible substrates

Hong Po[1], Corentin Dabard[1], Benoit Roman[2], Etienne Reyssat[2], José Bico[2], Benoit Baptiste[3], Emmanuel Lhuillier[4], Sandrine Ithurria[1,*]

[1] Laboratoire de Physique et d'Etude des Matériaux, ESPCI-Paris, PSL Research University, Sorbonne Université UPMC Univ Paris 06, CNRS, 10 rue Vauquelin 75005 Paris, France

[2] Physique et Mécanique des Milieux Hétérogènes, ESPCI-Paris, PSL Research University, CNRS, Université de Paris, 75005 Paris, France

[3] Sorbonne Université, CNRS, Institut de minéralogie, de physique des matériaux et de cosmochimie, IMPMC, F-75005 Paris, France

[4] Sorbonne Université, CNRS, Institut des NanoSciences de Paris, INSP, F-75005 Paris, France

* Corresponding author: sandrine.ithurria@espci.fr

Abstract

The crystal structure of atomically defined colloidal II-VI semiconductor nanoplatelets (NPLs) induces the self-assembly of organic ligands over thousands of nm^2 on the top and bottom basal planes of these anisotropic nanoparticles. NPLs curl into helices under the influence of the surface stress induced by these ligands. We demonstrate the control of the radii of NPLs helices through the ligands described as an anchoring group and an aliphatic chain of a given length. A mechanical model accounting for the misfit strain between the inorganic core and the surface ligands predicts the helices radii. We show how the chirality of the helices can be tuned by the ligands anchoring group and inverted from one population to another.

Keywords: nanoplatelets, curling, nanomechanic, ligands, diffraction

Introduction

Colloidal II-VI semiconductor nanoplatelets (NPLs) have emerged as promising materials for optoelectronic devices[1,2] thanks to their exceptionally narrow optical properties tunable from the visible to the near IR.[3–5] Such thin nanoparticles exhibit an additional original feature: their mechanical flexibility. Indeed, while considered as 2D nanoparticles in the sense of electronic confinement, NPLs may curl into chiral twists or helices. It has been shown that circularly polarized light may be produced using an assembly of twists.[6] Hence, the chiral shape of such particles is predicted to favor these peculiar optical properties.[7,8] At the nanoscale, surface chemistry is a tool of choice to control the NPLs shape.[9–13] For instance, NPLs unfold as their surface is covered with halides ligands co-stabilized by amines.[11] In that respect, in addition to the tuning of NPLs core composition or the synthesis of heterostructures,[14] surface chemistry appears as a promising tool for the design of original optical properties for those nanomaterials.

The NPLs thickness presents a subatomic roughness over thousands of nm^2, thus these nanosheets can be assimilated to flexible substrates for the self-assembly of molecules (SAM). SAMs are usually studied on thick metallic substrates[15–17] in which, despite a reorganization of the surface atoms, their geometry is maintained.[18,19] Other thin nanomaterials such as graphene or transitions metal dichalcogenides can bend under residual stresses.[20,21] However, they are less versatile than II-VI semiconductor NPLs, whose thickness, composition and lateral dimensions can be varied to tune their optical properties. The match between nanomaterials defined at the atomic scale, their crystal structure and their surface chemistry render the II-VI semiconductor NPLs with yet no equivalent.

Here, we control the shape of NPLs by thiolates surface ligands with 2 to 18 carbon long aliphatic chains.[13,22] These exchanges are performed on NPLs of various thicknesses and compositions to tune their curvature and are characterized by microscopy and X-Ray diffraction. We propose a minimal mechanical model which takes into account the inorganic core, the anchoring group of the ligands and the aliphatic chains to predict the curling of NPLs and the radius of the resulting helices. The order of magnitude of the observed helices radii indicates a 20% mismatch between the inorganic core NPLs and their surface ligands. The average deformation of the zinc blende core structure remains however moderate (below 1%).

Results and discussion

CdSe NPLs are anisotropic nanocrystals with a thickness $\approx$ 1 nm and lateral dimensions ranging from tens to hundreds of nm with a zinc blende crystal structure of lattice parameter a_c (a_c(CdSe)=6.05 Å[23]). They present a rectangular shape whose length, width and thickness are in the <100> directions. Due to a $\bar{4}$ axis along their thickness, the top and bottom $\{001\}$ and $\{00\bar{1}\}$ facets are chemically equivalent but oriented at 90° from each other (**Figure 1a**). Consequently, the bound surface ligands induce orthogonal stresses on opposite facets and the inorganic core/surface ligands dimensional mismatch costs elastic energy.[13,24] As a result of energy minimization, the narrowest NPLs form twisted ribbons while wider NPLs, discussed in this work, coil into cylindrical helices (**Figure 1a**)[25].

Here, CdSe NPLs with thickness ranging from 3 to 7 monolayers (MLs), 4 ML CdS NPLs and CdSe/CdS core/shell NPLs with large lateral dimensions (100-500 nm) are synthesized (NPLs with N MLs possess $N+1$ cationic planes alternated with N chalcogenide planes in their thickness.[26–28] Native

carboxylate ligands are exchanged with thiolates $C_nH_{2n+1}S$ ligands (n= 2 to 18) in a two-step process to ensure a complete surface chemistry change (**Supp Info Figure S1-S8, Table S1-S10**). The exchange is confirmed by elemental analysis and FTIR spectroscopy. The characteristic peaks of the carboxylates around 1525 cm^{-1} and 1420 cm^{-1}, corresponding to their asymmetrical and symmetrical vibrations, disappear with the exchange by the different alkanethiolates. The appearance of new peaks at around 700 cm^{-1}, confirms the presence of carbon-sulfide bonds in the system (**Supp Info Figure S1**). In absorption (**Figure 1b**), these exchanges induce a redshift of the two optical transitions attributed to the heavy (resp. light) hole to conduction band transitions from 463 nm (resp. 433 nm) for carboxylates capped 3 ML CdSe NPLs to 494 ± 1 nm (resp. 470 nm) for thiolates capped 3 ML CdSe NPLs.[3,10,22] The redshift of the optical features arises from two effects: (i) the partial delocalization of the exciton wavefunction over the sulfide planes and (ii) a change from a contractile strain to an extensional strain in the thickness direction which induces an increase in the lattice parameter and a decrease of the confinement.
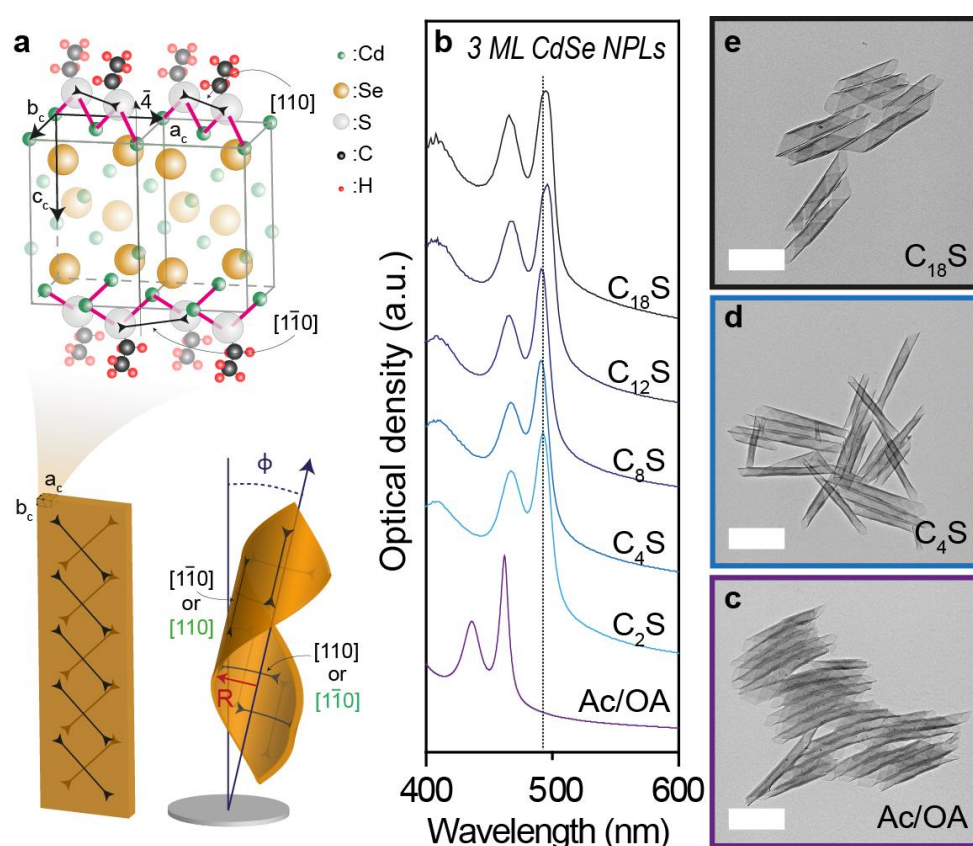

Figure 1: *(a) CdSe zinc blende crystal structure in a 3 ML CdSe NPL. The arrows illustrate the compressive stress brought by ethanethiolates ligands. The presence of a $\bar{4}$ axis along the NPL thickness induces compressive stress on top and bottom wide facets oriented at 90° from each other. The internal elastic energy is minimized as a wide NPL curls into a helix. This latter is defined by its radius R and its axis is tilted by an angle of ϕ to the normal plane (b) Absorption spectra of 3 ML CdSe NPLs capped with Acetate/Oleate, and C_nS ligands (where C_n : $C_nH_{2n+1}S^-$ and n=2, 4, 8, 12, 18). (c), (d) and (e) TEM images of 3 ML CdSe NPLs capped with Acetate/Oleate (purple frame), with $C_4H_9S^-$ (blue frame) and with $C_{18}H_{37}S^-$ (black frame). Scale bar: 200 nm*

The transmission electron microscopy (TEM) pictures (**Figure 1 c-e**) unveil helices with radius *R* increasing from 6.5 nm to 13 nm as the aliphatic chain length increases from 2 to 18 carbons.[22] The pristine helical NPLs capped with a mixture of acetate and oleate ligands present a radius *R* ~ 9 nm similar to dodecanthiolates capped NPLs (**Supp Info Figure S1**). While similar variations have been

observed with CdSe NPLs ranging from 3 MLs to 7 MLs, thicker cores result into larger helices radii (**Figure 2a, Supp Info Fig S1-S8**). Predicting and being able to tune the radius of the helix is of particular interest as theoretical studies show that circularly polarized optical properties should emerge from curled NPLs of various radii (**Supp Info Fig S9**).[7,29] Interestingly, similar predictions have been proposed for the helicoidal assemblies of nanocrystals obtained through interactions between surface chiral ligands and circularly polarized light.[30–32]

Here, thiolate groups bridge two surface cadmiums to provide a tetrahedral environment.[10,33] Sulfides induce compressive stress both in the $[110]$ and $[1\bar{1}0]$ directions on the two opposite wide facets of CdSe NPLs. Thus NPLs curl with their top or bottom facets inside the helices with equal probability (**Figure 1a, Supp Info Figure S10-S11**).[10,33] When wide enough, NPLs take the geometry of strips cut out from a cylinder with a single principal curvature in the $[110]$ direction.[25] At equilibrium, within NPLs helices, an atomic scale elemental volume derived from the zinc blende crystal structure has a constant curvature resulting from the lattice mismatch generated by thiolate ligands in the $[110]$ direction (**Figure 2a**). Converserly, the mismatch in the $[1\bar{1}0]$ direction plays no role in the bending. In the $[110]$ direction, the lattice parameter a, varies linearly across the thickness of the helix from a' to a'', with an average value of $|a_0| = a_c \sqrt{2}/2$ (a_c is the zinc blende lattice parameter of CdSe). Perpendicular to a, in the $[1\bar{1}0]$ direction the parameter b_0 remains constant along the thickness c of the NPLs ($|a_0| = |b_0|$).

In mechanics, the curvature κ (=$1/R$) , due to a strain mismatch $\Delta\varepsilon$ at the interface between two layers of thicknesses H and h and Young moduli E_s and E_d, is predicted by the classical model from Timoshenko.[34,35] For 3 ML CdSe NPLs capped with sulfides, the thicknesses H and h of CdSe and the sulfide layer would respectively be 6 and 1 atomic planes (1 atomic plane is 1.5 Å thick) (**Figure 2b**). The outside sulfide layer is neglected, as these sulfide groups bound to the cadmiums atoms in a direction perpendicular to the curvature so that they do not interfere with it. The Young moduli are taken as those of bulk CdSe and CdS (E_s(CdSe)=40 GPa and E_d(CdS)=46 GPa)[36] and $\Delta\varepsilon$ is estimated from their lattice mismatch (-3.8%). However, with these values the calculated radius is one order of magnitude larger than experimentally measured $R_{exp} \approx 6$ nm for 3 ML CdSe NPLs capped with ethanethiolates. Actually, only a large misfit strain $\Delta\varepsilon \approx$ -20% would account for such a large curvature.
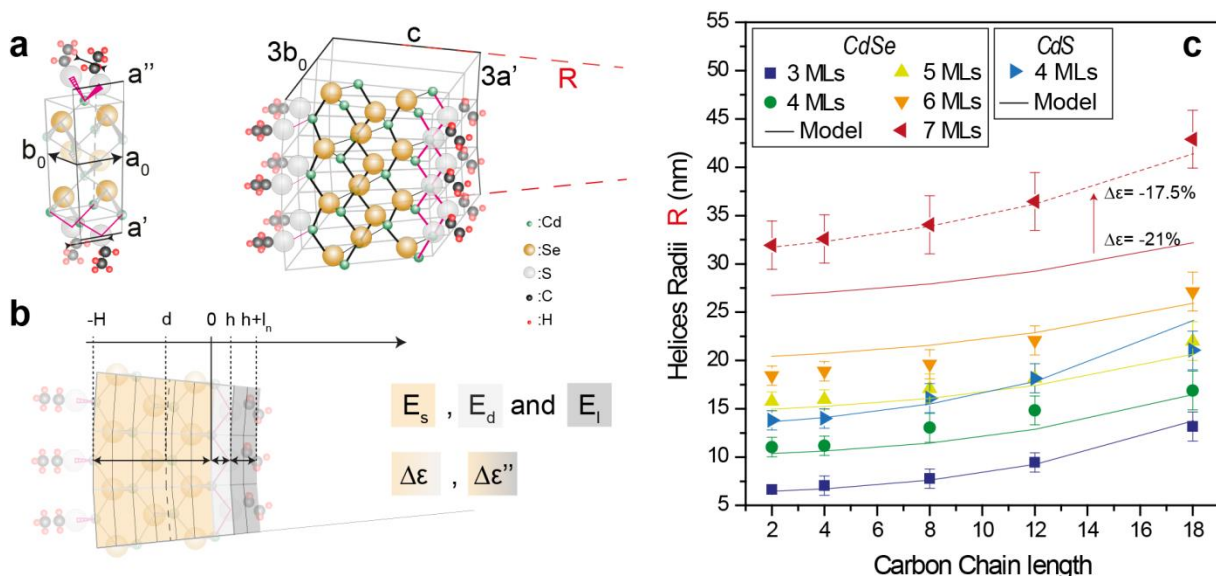
Figure 2: (a) Sketch of an elemental volume in a 3ML helical NPL. The thickness c of the NPL takes into account the sulfide head group of ligands. The two other lattice parameters, a_0 and b_0, defined at the mid-plane of the NPL, are respectively perpendicular and parallel to the helix axis and are in the $[110]$ and $[1\bar{1}0]$ directions of the zinc blende crystal structure (stress directions), with $|a_0| = |b_0| = a_c \sqrt{2}/2$. In the c direction, the atomic planes are separated by the same distance ($a_c/4$). The parameter a varies from a' to a'', geometrically defined by the expression (R-c/2)/R=a'/a₀ and (R+c/2)/R=a''/a₀, where R is the radius of the helix determined by TEM. b_0 remains constant through the thickness of the NPLs. In the model, the adjustable parameters are H, h, and l_n, the thicknesses of CdSe, S layer and the chains length, E_s, E_d and E_l the Young moduli of CdSe, S layer and the aliphatic chain and $\Delta\varepsilon$ and $\Delta\varepsilon''$ the mismatches between CdSe and the surface sulfides and CdSe and the aliphatic chains. On the right, we sketch a 3x3 elemental volume which represents a portion of cylindrical helix. (b) Projection of a piece of helix, showing the dimensions of the different parts considered in the three-layers-misfit-strains model (c) Experimental helices radii deduced from the TEM images for CdSe NPLs with thicknesses ranging from 3 to 7 MLs and 4 ML CdS NPLs (average over 50 helices). The lines are the helices radii predicted from the mechanical model.

The S-Cd distance, at the NPL-ligand interface, is drastically reduced when compared to the case of a sulfide atom in a tetrahedral environment with four identical Cd neighbors. This is explained by the electrostatic interactions between the thiolate anchoring group and the positively charged Cd surface (**Supp Info Figure S12**).[15] Although the order of magnitude of the curling radius of CdSe and CdS NPLs evidences unexpectedly strong surface stresses induced by thiolates, this strong interaction does not explain the variation of the helices radii with the length of the ligands (**Figure 2c**). It thus seems reasonable, at first order, to consider a constant mismatch between the inorganic core and the sulfide layer, independent of the aliphatic chains length as the energetic level of the sulfide orbitals involved in the bridging should be independent of the length of aliphatic chains. Secondly, it is essential to consider the steric effect of the organic tails of ligands whose thickness can be larger than the inorganic NPLs.

We build up on the classical work of Timoshenko and propose a model involving 3 main layers, namely inorganic core (CdSe), anchoring groups (S) and aliphatic chains inside the helix (**Figure 2a, Supp Info Figure S13**). Hence, in addition of the previous parameters, we should consider the thickness of the ligand alkyl chain l_n, its Young modulus E_l and the mismatch $\Delta\varepsilon''$ between CdSe and the aliphatic chains. The chains thickness is assumed to be n times the intercarbon distance estimated at 1 Å (**Supp Info Figure S14-S15**). We consider compressive Young modulus of the carbon chains equal to 0.9 GPa. This value is derived and comparable to the estimation of bending moduli done on carbon chains constituting lipid bilayers, of the order of 10^{-19} J.[37] It reflects the steric hindrance imposed by the packing density of ligands. Note that since chains in the outer side of the helix are uncompressed, they are not taken into account. This Young modulus may be overestimated for smaller aliphatic chains, but due to its smaller thickness, its effect on the estimated helices radii is also lowered (**Supp Info Figure S14**). Finally, $\Delta\varepsilon$ is adjusted and set to -21%, to obtain a good agreement between the model and the 3 ML CdSe NPLs with the shortest aliphatic chains.

The mismatch $\Delta\varepsilon''$ between the aliphatic chain and CdSe is defined from the maximum packing density of chains. On the {001} zinc blende facet of the NPLs, there is one ligand (*i.e.* one aliphatic chain) per cadmium surface with a density of 1 Cd/18.3 Å². Experimentally, it has been shown on a Langmuir Blodgett film, that the maximum density of thiolates is 1 thiolate/18.5 Å²,[38] we thus assume $\Delta\varepsilon'' = 0\%$. To conclude, the thiolate anchoring group brings a strong compressive stress on both CdSe and CdS core, while the aliphatic chain brings a tensile stress to the thiolate. Therefore, in a population of NPLs, smaller radii should be expected and is effectively observed for the shortest aliphatic chains (**Figure 2c**).

The predictions of this simplified model are in excellent agreement with the experimental measurements of helices radii, for increasing NPLs thicknesses from 3 to 6 MLs (**Figure 2c**). For thicker 7 ML CdSe NPLs, a better fit is obtained for $\Delta\varepsilon = -17.5\%$, but defects in the inorganic NPLs may also explain the larger experimental radii. The growth of NPLs in their thickness is done by colloidal Atomic Layer Deposition which may lead to defects. Possible missing surface cadmiums are accompanied by vacancies of ligands, which will hence reduce the induced surface stress and result in larger helices radii. In other words, the absolute effective value of $\Delta\varepsilon$ is reduced. Concerning CdS, since the lattice mismatch between CdS and CdSe bulks is of 3.8%, an equivalent increase is applied to $\Delta\varepsilon$ (=-17.2% (-21%+3.8%)). Again, the resulting fit is in good agreement with the experimental values (**Figure 2c**, **Supp Info Figure S16-S17**). Thus, this macroscopic model predicts well the curling of NPLs. It reveals a major effect of the surface chemistry and the strong coupling of the ligands to the Cd surface atoms.

The model also enables to predict the strain in different atomic planes of the NPL. The inner side of the helix, presents a contractile strain while the outer is extended. For the different aliphatic chains lengths, the strain in the middle of the thickness almost vanishes. In other words a_0 remains the same, but the amplitude of the strain varies along the rest of the sectioning. This is further verified by X-Ray diffraction.

Figure 3a and 3f present the diffraction patterns of 3 ML CdSe NPLs capped with thiolate ligands acquired on two diffractometers. In the first experiment, the NPLs in hexane are placed in a capillary and the 2D detectors shows Debye-Scherrer rings (**Figure 3c**). In the second experiment, the NPLs are dried on a substrate, and the diffracted patterns are acquired on a θ-2θ configuration (**Figure 3d**). In both cases, the diffractograms exhibit Bragg peaks around 25°, 42° and 50°, attributed to the (111), (220) and (311) families of planes in a zinc blende crystal structure. These peaks are broad due to the finite size of NPLs, and asymmetric. In solution, the NPLs diffractions show minor differences while changing the ligands from ethanethiolates to octadecanethiolates (**Figure 3a**). All of them present a narrow and broad contribution around 42°. In the second experiment, such narrow peaks are not observed, instead there is a doublet of peaks (**Figure 3f**), which broadens with shorter aliphatic chain lengths.
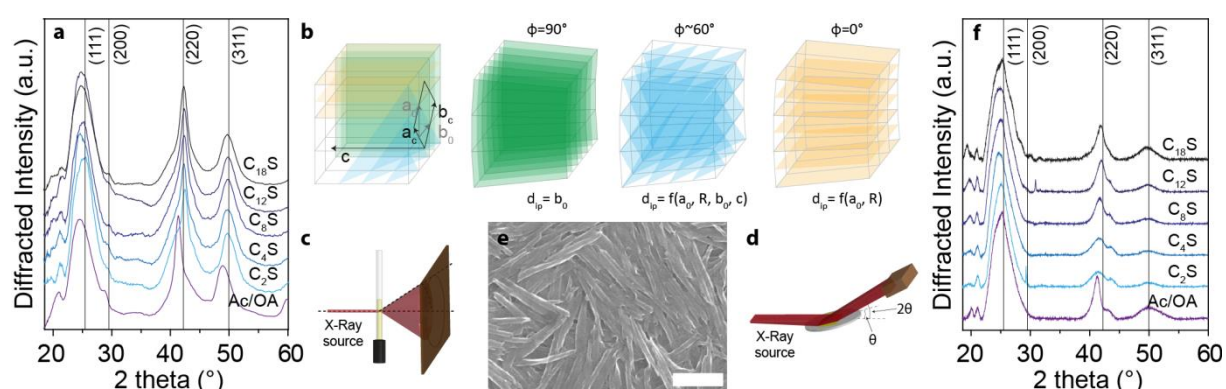
Figure 3: *(a) X-Ray diffractograms of 3 ML CdSe NPLs suspended in hexane capped with Acetate/Oleate, and C_nS ligands (where C_n : $C_nH_{2n+1}S^-$ and n=2, 4, 8, 12, 18). The source is a Mo tube but the data have been plotted as if it was a Cu source to ease comparison (Raw data are in **Supp Info Figure S19**). Vertical lines represent the Bragg angle for zinc blende CdSe of a_c=6.05 Å (b) Elemental volume of an unfolded NPLs showing the equivalent (220)*

planes. The planes are now represented in a piece of helix. The green planes present a constant interplanar distance equal to b_0. The blue planes present an average interplanar distance which depends on a_0 and R, b_0 and c. The orange planes present an average interplanar which depends on a_0 and R. (c) and (d) Sketch of the experimental setups. In (c), the NPLs are suspended in hexane in a capillary and the diffracted beam insulates a 2D detector. In (d), the NPLs are deposited on a zero back-scattering Si substrate. It defines a θ-2θ configuration. (e) Scanning Electron Microscopy picture of 3 ML CdSe NPLs with thiolate ligands. It shows the specific orientation of the NPLs helices on the substrate, scale bar: 500 nm. (f) X-Ray diffraction of 3 ML CdSe NPLs deposited on a substrate capped with Acetate/Oleate, and C_nS ligands (where C_n : $C_nH_{2n+1}S^-$ and n=2, 4, 8, 12, 18). The X-Ray source is the Cu- Kα radiation

Owing to their helicoidal shape, the dried NPLs helices preferentially lay down on the substrate, as observed on the SEM image (**Figure 3e**). Therefore, some planes will diffract with a high probability while other would not (**Supp Info Figure S20**). As an example, the equivalent (220) planes in unfolded zinc blende NPLs split into three contributions in a helix (**Figure 3b**). The first contribution presents an interplanar distance equal to b_0 and is independent of the helix radius (green planes in **Figure 3b**). These planes diffract in a θ-2θ set up, only if the helix axis is normal to the substrate (ϕ=90°), which is unlikely. The second family of planes (in blue in **Figure 3b**) diffracts when the helix axis presents an angle ϕ around 60°, also unlikely. Finally, the orange family of planes in **Figure 3b** presents an interplanar distance dependent on a, which varies from a' and a''. They diffract when the helix axis is parallel to the substrate (ϕ=0°), as in a θ-2θ set up. In the first XRD experiments, all these planes diffract, and, the broad feature at 2$\theta \approx$ 42° is more complex than expected. Nevertheless, the narrow peak can be attributed to the family of planes with constant b_0 interplanar distance. It barely varies with the thiolate ligands and is close to 4.28 Å, the expected value for a zinc blende structure with a_c= 6.05 Å[23] (**Supp Info Figure S18**).

To verify such assumptions, we have simulated the X-Ray intensity diffracted by flat 8 nm x 8 nm 3ML CdSe NPLs, and helices. In the NPLs, the atomic positions are generated such that $|a_0| = |b_0| = a_c \sqrt{2}/2 = 4.28$ Å, and a' and a'' are estimated from the helix radius R. The observations from the first experiment are in excellent agreement with simulated diffractograms, using the Debye formula (**Figure 4a**). An increase of the helix radius smoothens the diffractograms and changes the intensities ratio between the peaks. It appears that despite stresses induced by the ligands are at the origin of the curling, the NPLs mostly preserve the zinc blende crystal structure (**Supp Info S18**).
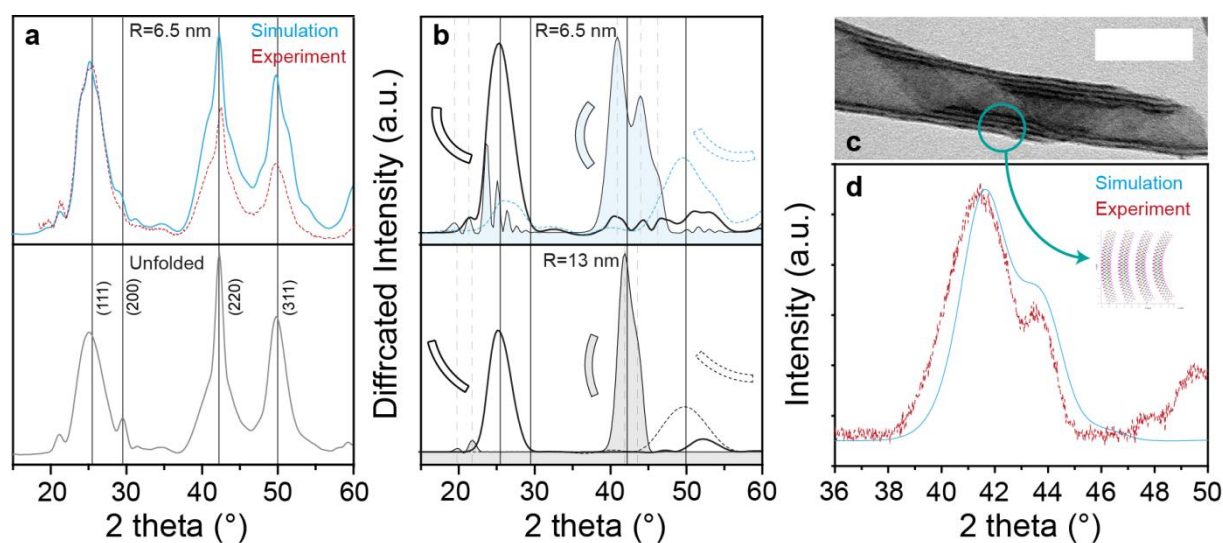
Figure 4: (a) Simulated (blue line) and experimental (dashed line) X-Ray diffractograms for isotropic diffraction (as in the 1st X-Ray experiment) on a piece of helix with a radius R=6.5 nm as for 3 ML CdSe NPLs capped with ethanethiolate ligands. The vertical lines represent the positions of diffracted peaks for a zinc blende crystals structure with a lattice parameter of a_c=6.05 Å. (b) Simulated diffractograms mimicking helices capped with ethane- and octadecane-thiolate ligands. The piece of helix is oriented at 3 preferential positions with respect to the incident X-Ray beam, to selectively represent the (111), (220) and (311) families of planes contributions. The vertical lines indicate the associating peaks centered around 25°, 42° and 50°. (c) TEM picture of 3 ML CdSe NPLs capped with octanethiolates ligands. The helix makes up to 4 turns within a single NPL. Scale bar is 50 nm. (d) Fitting (blue line) of the experimental doublet (red dash line) observed at 2θ around 42° in the 2nd diffraction experiment. The inset shows the pieces of helices considered for the simulations.

This evolution of the diffractogram is further confirmed with simulations that model the diffraction from the θ-2θ configuration. Now, in the simulations, the helices are specifically oriented with respect to the incident beam such that the (111), (220) and (311) planes are parallel to the substrate and diffract willingly (**Figure 4b, Supp Info Figure S21**). **Figure 4b** presents the intensities diffracted by 6.5 nm and 13 nm radii helices. As in the experiments, the most noticeable difference comes from the peak around 42° (**Figure 3f**). For the 6.5 nm helix radius, there is a triplet of peaks while for the 13 nm one, only a doublet of peaks is obtained. Surprisingly, none of these peaks are centered at 42.2°, which is the expected angle for a family of planes separated by a_0=4.28 Å, as in CdSe bulk. Indeed, even though the mean interatomic distance is a_0 along the thickness direction, they appear more dispersed in size as the helix radius becomes smaller. Hence, the value a_0 is not more likely to appear than others (**Supp Info Figure S22**). Finally, the experimental data are fitted taking into account the multiple turns of the NPLs (**Figure 4d, Supp Info Figure S23**). Indeed, in large lateral dimensions NPLs, there can be up to 4 turns in a single helix (**Figure 4c**). Thus, the radii of the helices take several values even within the same NPL. Although the surface stress induced by thiolate ligands is strong, the average in-plane lattice parameter is that of zinc blende CdSe. Out of plane, across the thickness, the induced strain is also negligible. Indeed, mechanically, the strain in a direction perpendicular to the surface in-plane stress cannot exceed this latter (**Supp Info Figure S24**).

Interestingly, the carboxylate-capped CdSe NPLs exhibit a positive strain of the in-plane lattice parameter which originates from a tensile stress brought by the ligands. In that case, the stress at the origin of curling is perpendicular to the helix axis on the outer surface of NPLs. Thus, the exchange from carboxylates to thiolates ligands demonstrates a change from a tensile stress to a compressive stress and therefore an inversion of the handedness of the NPLs helices (**Supp Info Figure S25-S26**).

Conclusion

In summary, II-VI semiconductor NPLs are flexible substrates that react promptly to various surface chemistries by adapting their shape. Employing a three-layers-misfit-strains mechanical model enables one to predict the bending of NPLs resulting from surface ligand adsorption. The model treats the anchoring group and the aliphatic chains contributions separately and demonstrates good agreement for all studied NPLs. We find that the electrostatic interactions between the inorganic core and the anchoring group of ligands induce a strong misfit superior to 20%. We show that accounting for the steric repulsion between the aliphatic chains of the ligands allows for fine tuning of the curvature of NPLs by playing on the length of the chains. The self-assembly of aliphatic chain of ligands is equivalent to a layer of Young modulus in lateral compression

in the order of 1 GPa. Ultimately, NPL or assemblies of NPLs with a single handedness could be used for enantioselective reactions, sensors, or source of circularly polarized light.

Experimental Section

<u>Chemicals</u>

Octadecene (ODE) (Sigma-Aldrich, 90%), cadmium acetate anhydrous (Cd(Ac)$_2$) (Sigma-Aldrich, 99.995%), cadmium oxide (CdO) (Strem Chemicals, 99.99%), myristic acid (Sigma-Aldrich, 99%), selenium powder (Se) (Strem Chemicals, 99.99%), sulphur powder (S) (Sigma, 99.99%), oleic acid (OA) (Sigma-Aldrich, 90%), ethanethiol (Fluka, >98%), butanethiol (Aldrich-Chemistry, 99%), octanethiol (Fluka, >97%), dodecanethiol (Aldrich-Chemistry, >98%), octadecanethiol (Aldrich-Chemistry, 98%), trioctylphosphine (TOP) (Alfa Aesar, 90%), tributylphosphine (TBP) (Cytec, Solvay), cadmium chloride hydrate (CdCl$_2$·xH$_2$O) (Sigma-Aldrich, 99.995%), cadmium iodide hydrate (CdI$_2$·xH$_2$O) (Aldrich-Chemistry, 99%), sodium tetrahydroborate (NaBH$_4$) (Sigma, 99%), sodium sulphide nonahydrate (Na$_2$S·9H$_2$O) (Aldrich-Chemistry , >99.99%), toluene (VWR, 99.5%), n-hexane (VWR, 99%), ethanol (VWR, 96%), methanol (Carlo Erba, 99.9%), N-methylformamide (NMF) (Carlo Erba, 99%), ammonia solution (28%, Aldrich-Chemistry)

<u>Preparation of Precursors</u>

Cadmium myristate (Cd(Myr)$_2$) In a three-neck flask, 2.56 g (20 mmol) of CdO and 11 g (50 mmol) of myristic acid are mixed and degassed at 70 °C during 30 min. Next, the heating temperature is increased to 200 °C under argon flow until the solution turns colourless. 30 mL of methanol is added to solubilize the excess MA at 60°C. The final product is precipitated with methanol and the washing process is repeated three times before being left to dry under vacuum at 70°C overnight.

Cadmium dithiolate (Cd(C$_n$H$_{(2n+1)}$S)$_2$) In a centrifuge tube, 1.83 g (10 mmol) of Cd(Cl)$_2$ is dissolved in a 30 mL solution consisting of an equal volume mix of Milli-Q H$_2$O and ethanol. Approximately 10 mL of ammonia solution are added dropwise under constant stirring, until the solution turns colorless. For each linear carbon chain (n = 2, 4, 8, 12, 18), 20 mmol of thiol solutions are introduced dropwise with the formation of white precipitates. At the end of addition, the mixture is stirred for 2 h before being washed twice with an equal amount of Milli-Q H$_2$O and ethanol. The final product is dried under vacuum at 70 °C overnight.

Trioctylphosphine selenide solution (TOPSe) 1M In a glove box, 20 mL of trioctylphosphine and 1.58 g (20 mmol) of selenium powder are stirred overnight until a colourless solution is obtained. This final product is later stored in the glove box in order to prevent it from oxidizing.

Sulfide octadecene solution (SODE) 0.1M In a three-neck flask, 100 mL of ODE is degassed at 70 °C during 30 min. Later under argon, 480 mg (15 mmol) of sulfur powder are added and the mixture is heated at 140 °C, up to a point where it turns slightly yellowish and clear. This solution is then cooled and stored at room temperature.

<u>Synthesis and Growth of NPLs</u>

Synthesis of 3 MLs CdSe large NPLs In a three-neck flask, 260 mg (1.1 mmol) of Cd(Ac)$_2$ is introduced before adding in 10 mL of ODE and 0.25 mL of OA. The mixture is heated at 70 °C under vacuum for

15 min. In a syringe, 0.6 mL (0.6 mmol) of TOPSe at 1 M diluted in 4.4 mL of ODE is prepared. Under Argon flow, the heating temperature is then increased to 190 °C and the Se precursor is injected at a rate of 1.25 mL/h. The solution gets more tainted in yellow as time goes on. At the end of injection, the heating mantle is removed to allow complete cooling of the reaction medium to room temperature. In order to precipitate the NPLs, equal amounts of ethanol and hexane are introduced during washing. At the end, the pellet of NPLs is suspended in 10 mL of hexane for further use.

Synthesis of 4MLs CdSe small NPLs In a three-neck flask, 24 mg (0.3 mmol) of Se powder and 340 mg (0.6 mmol) of Cd(Myr)$_2$ are poured. 20 mL of ODE are then introduced before heating the mixture at 70°C under vacuum for 15 min. The temperature is later increased to 240 °C under argon and when the mixture turns orange around 200 °C, 110 mg (0.5 mmol) of Cd(Ac)$_2$ are rapidly added. The reaction is continued under constant stirring during 10 min. At the end, the reaction medium is cooled to room temperature after adding 0.5 mL of OA. Similar washing steps as in the previous case are used to separate synthesized dots and NPLs. At the end, the pellet of NPLs is rsuspended in 10 mL of hexane for further growth into larger NPLs.

Lateral growth of NPLs In a three-neck flask, 201 mg (0.9 mmol) of Cd(Ac)$_2$ is introduced in order to increase the surface area of the initial NPLs by approximately a factor of 25. 10 % of previously synthesized 4 MLs CdSe small NPLs of around (30x6) nm^2 are precipitated in a mixture of ethanol and hexane, before being suspended in 6 mL of ODE. This latter is added into the flask containing 0.3 mL of OA and heated at 70 °C under vacuum for 15 min. A growth solution consisting of 0.375 mL (0.375 mmol) of TOPSe at 1M diluted in 0.125 mL of ODE is prepared in a syringe. The heating temperature is then increased to 230 °C under argon, at which the injection of growth solution occurs at a rate of 0.125 mL/h. The solution turns darker as time goes on. At the end of reaction, equal amounts of ethanol and hexane are used during washing. At the end, the pellet is suspended in 5 mL of hexane for further use.

c-ALD growth towards thicker 5, 6 and 7 MLs CdSe large NPLs The precursors of selenium are prepared by reducing selenium powder in a solution of NMF and ethanol, in the presence of NaBH$_4$. In order to grow 5 MLs CdSe NPLs for instance, 10 % of as-synthesized 3 MLs CdSe NPLs are taken as starting materials. The introduction of selenium ions onto the surface of existing NPLs in the presence of TBP induces their precipitation in hexane. This latter is then resuspended in NMF and washed in toluene, before the surface addition of cadmium precursors. These NPLs are finally annealed in the presence of 25 ml of Cd(Ac)$_2$, 35 μL of OA, 45 μL TBP and 4 mL of ODE at 230 °C. At the end of reaction, similar washing steps are carried out and the pellet is suspended in 5 mL of hexane for further ligands exchange.

c-ALD growth of core/shell CdSe/CdS NPLs As previously, 10 % of as-synthesized 3 MLs CdSe NPLs suspended in hexane are withdrawn, and the precursors of sulphur are added. The addition of Na$_2$S dissolved in a solution of NMF and ethanol, induces the transfer of nanoparticles into the polar solvent. These NPLs are then washed and resuspended in NMF, before the surface addition of cadmium precursors. They are introduced in the form of Cd(Ac)$_2$ accompanied by OA to retransfer the nanoparticles back into the apolar solvent. These steps could be repeated in order to grow thicker CdS shells onto existing CdSe core structures.

Synthesis of 4 MLs CdS NPLs In a three-neck flask, 240 mg (1 mmol) of Cd(Ac)$_2$ are placed before adding in 10 mL of ODE and 0.2 mL of OA. The mixture is degassed at 70 °C under vacuum for 15 min. The heating temperature is then increased to 210 °C under argon, at which the injection of 6 mL (0.6

mmol) of SODE at 0.1 M takes place, at a rate of 1.5 mL/h. At the end of injection, heating is removed to enable complete cooling of the reaction medium down to room temperature, before washing the nanoparticles in a mixture of hexane and ethanol. The pellet in the end, is suspended in 10 mL of hexane for further use.

Surface ligands exchange

From carboxylates to thiolates: For each population of NPLs, the quantity of nanoparticles solution withdrawn to be used for ligands exchange purpose is calculated to contain approximately 4 µmol of surface cadmium ions. For instance, 0.1 mL of as-synthesized 3MLs CdSe NPLs are placed in a test tube, in which 100 equivalences of thiolate ligands in respect of surface cadmiums are added. These ligands are introduced under the form of a linear carbon chain, presenting a thiol group at only one of its ends. Identical steps are carried out for five different carbon chain lengths, using ethanethiol (n=2), butanethiol (n=4), octanethiol (n=8), dodecanethiol (n=12) and octadecanethiol (n=18). Upon addition of thiol ligands into solutions of NPLs, the test tubes are sealed and placed in an oven at 60°C for the exchange process to take place in hexane overnight. The nanoparticles are later washed in an equal amount of ethanol and hexane, before annealing in the presence of 2 equivalences of cadmium dithiolate respective to each carbon chain length for each sample at 160 °C during 10 min. Similar washing steps are then done and the pellet is resuspended in 5 mL of hexane for further characterizations.

Characterization techniques

TEM analysis Transmission electron microscopy (TEM) images are recorded on a JEOL 2010 transmission electron microscope at a working voltage of 200 kV. The images of nanoparticles are later analyzed under ImageJ and information on their coiling radii distribution is obtained over a population of 50 helices (all the values are in nm). **Table 1** summarizes the diameters and standard deviations for the different surface chemistries of all the synthesized NPLs.

	C_2S	C_4S	C_8S	$C_{12}S$	$C_{18}S$	Ac/OA
3 ML CdSe	13.1 ± 1.6	13.9 ± 2.7	15.3 ± 2.0	18.7 ± 3.1	26.0 ± 2.9	18.8 ± 2.9
4 ML CdSe	21.7 ± 1.9	22.1 ± 2.1	25.8 ± 2.3	29.3 ± 2.2	33.3 ± 3.3	33.5 ± 2.7
5 ML CdSe	31.1 ± 4.3	31.5 ± 2.3	33.8 ± 3.3	35.9 ± 3.9	43.4 ± 4.3	40.4 ± 4.6
6 ML CdSe	42.8 ± 2.7	42.1 ± 3.0	43.0 ± 1.7	46.1 ± 2.8	53.6 ± 3.7	
7 ML CdSe	63.0 ± 5.6	64.4 ± 5.9	67.3 ± 4.2	72.0 ± 4.8	84.8 ± 8.5	81.2 ± 7.9
5ML CdSe$_3$/CdS$_1$	35.6 ± 4.8	35.6 ± 4.2	39.2 ± 6.4	43.2 ± 3.6	55.8 ± 5.1	44.4 ± 5.8
7 ML CdSe$_3$/CdS$_2$	63.0 ± 8.5	63.0 ± 8.3	66.7 ± 8.6	69.5 ± 6.7	82.2 ± 8.2	66.9 ± 7.7
4 ML CdS	27.6 ± 3.7	28.0 ± 2.6	32.2 ± 3.2	36.4 ± 2.6	42.1 ± 4.3	21.5 ± 2.1

Table 1 : *Average diameter and standard deviation of 3 ML CdSe NPLs, 4 ML CdSe NPLs, 5 ML CdSe NPLs, 6 ML CdSe NPLs, 7 ML CdSe NPLs, 5 ML CdSe$_3$/CdS$_1$ NPLs, 7 ML CdSe$_3$/CdS$_2$ NPLs and 4 ML CdSe NPLs capped with Acetate/Oleate, and C$_n$S ligands (where C$_n$: C$_n$H$_{2n+1}$S$^-$ and n=2, 4, 8, 12, 18).*

SEM and EDX analysis Scanning electron microscopy (SEM) images are recorded with a FEI Magellan scanning electron microscope at a working condition of 18 kV in voltage and 0.40 nA in current. The energy-dispersive X-ray spectroscopy (EDX) signals are obtained through an Oxford Instrument detector mounted onto the microscope.

XRD analysis X-ray diffraction (XRD) signals of thin films of nanoparticles drop-cast on a (311)-cutted mono-crystalline silicon substrate are recorded on a Phillips X'Pert diffractometer with a Cu-Kα radiation. Measurements are performed at a working condition of 40 kV in voltage and 40 mA in current. Scattering patterns are obtained under the θ-2θ reflection mode of configuration, in the 2θ range between (10-60)° with a step size of 0.016°. Further XRD signals are as well recorded on a Rigaku MicroMax 007HF diffractometer with a Mo-Kα radiation. Experimental conditions of 50kV in voltage and 24mA in current are set. Diffraction patterns are obtained this time around, under the capillary mode where the nanoparticles are suspended in hexane as the organic solvent. Signal acquisitions are done in the 2θ range between (0.03-64.9)° with a step size of 0.030°. Raw data saved under the format of XRDML are later treated with HighScore application.

FTIR measurements Fourier transform infrared spectroscopy (FTIR) spectra are recorded on a Bruker Vertex 70 spectrometer at room temperature, in the wavenumber range between (400-4000) cm^{-1}. During measurements, concentrated nanoparticles colloidal solutions resuspended in toluene are drop-cast onto the detection zone and signals are acquired after solvent evaporation.

Optical measurements Absorption spectra are recorded at room temperature on a Shimadzu UV-1800 spectrophotometer. During measurements, small fractions are taken out from initial colloidal solutions of nanoparticles to be diluted in hexane to reach an optical density <3.

Associated content

The supporting information is available free of charge at…

Absorption spectroscopy, transmission electronic microscopy images and energy dispersive spectroscopy of core and core/shell NPLs. Qualitative and quantitative multi-layer-misfit strain materials model applied to NPLs. Validation of the mechanical model. X-Ray diffraction simulations.

Acknowledgments

References

(1)   Liu, B.; Altintas, Y.; Wang, L.; Shendre, S.; Sharma, M.; Sun, H.; Mutlugun, E.; Demir, H. V. Record High External Quantum Efficiency of 19.2% Achieved in Light-Emitting Diodes of Colloidal Quantum Wells Enabled by Hot-Injection Shell Growth. *Adv. Mater.* **2019**, *32* (8), 1905824.

(2)   Guzelturk, B.; Kelestemur, Y.; Olutas, M.; Delikanli, S.; Demir, H. V. Amplified Spontaneous Emission and Lasing in Colloidal Nanoplatelets. *ACS Nano* **2014**, *8* (7), 6599–6605.

(3)   Ithurria, S.; Tessier, M. D.; Mahler, B.; Lobo, R. P. S. M.; Dubertret, B.; Efros, A. L. Colloidal Nanoplatelets with Two-Dimensional Electronic Structure. *Nature Materials*. 2011, pp 936–941.

(4)   Izquierdo, E.; Robin, A.; Keuleyan, S.; Lequeux, N.; Lhuillier, E.; Ithurria, S. Strongly Confined HgTe 2D Nanoplatelets as Narrow Near-Infrared Emitters. *J. Am. Chem. Soc.* **2016**, *138* (33), 10496–10501.

(5)   Gréboval, C.; Izquierdo, E.; Livache, C.; Martinez, B.; Dufour, M.; Goubet, N.; Moghaddam, N.; Qu, J.; Chu, A.; Ramade, J.; Aubin, H.; Cruguel, H.; Silly, M.; Lhuillier, E.; Ithurria, S. Impact of Dimensionality and Confinement on the Electronic Properties of Mercury Chalcogenide Nanocrystals. *Nanoscale* **2019**, *11* (9), 4061–4066.

(6)   Jana, S.; De Frutos, M.; Davidson, P.; Abécassis, B. Ligand-Induced Twisting of Nanoplatelets and Their Self-Assembly into Chiral Ribbons. *Sci. Adv.* **2017**, *3* (9).

(7)   Rukhlenko, I. D.; Baimuratov, A. S.; Tepliakov, N. V.; Baranov, A. V.; Fedorov, A. V. Shape-Induced Optical Activity of Chiral Nanocrystals. *Opt. Lett.* **2016**, *41* (11), 2438.

(8)   Tepliakov, N. V.; Baimuratov, A. S.; Vovk, I. A.; Leonov, M. Y.; Baranov, A. V.; Fedorov, A. V.; Rukhlenko, I. D. Chiral Optical Properties of Tapered Semiconductor Nanoscrolls. *ACS Nano* **2017**, *11* (7), 7508–7515.

(9)   Mahler, B.; Nadal, B.; Bouet, C.; Patriarche, G.; Dubertret, B. Core/Shell Colloidal Semiconductor Nanoplatelets. *J. Am. Chem. Soc.* **2012**, *134* (45), 18591–18598.

(10)   Antanovich, A.; Achtstein, A. W.; Matsukovich, A.; Prudnikau, A.; Bhaskar, P.; Gurin, V.; Molinari, M.; Artemyev, M. A Strain-Induced Exciton Transition Energy Shift in CdSe Nanoplatelets: The Impact of an Organic Ligand Shell. *Nanoscale* **2017**, *9* (45), 18042–18053.

(11)   Dufour, M.; Qu, J.; Greboval, C.; Méthivier, C.; Ithurria, S. Halide Ligands to Release Strain in Cadmium Chalcogenide Nanoplatelets and Achieve High Brightness. *ACS Nano* **2019**, *13* (5), 5326–5334.

(12)   Shlenskaya, N. N.; Yao, Y.; Mano, T.; Kuroda, T.; Garshev, A. V.; Kozlovsky, V. F.; Gaskov, A. M.; Vasiliev, R. B.; Sakoda, K. Scroll-like Alloyed CdSxSe1-x Nanoplatelets: Facile Synthesis and Detailed Analysis of Tunable Optical Properties. *Chem. Mater.* **2016**, *29* (2), 579–586.

(13)   Vasiliev, R. B.; Lazareva, E. P.; Karlova, D. a.; Garshev, A. V.; Yao, Y.; Kuroda, T.; Gaskov, A. M.; Sakoda, K. Spontaneous Folding of CdTe Nanosheets Induced by Ligand Exchange. *Chem. Mater.* **2018**, *30* (5), 1710–1717.

(14)   Nasilowski, M.; Mahler, B.; Lhuillier, E.; Ithurria, S.; Dubertret, B. Two-Dimensional Colloidal Nanocrystals. *Chem. Rev.* **2016**, *116* (18), 10934–10982.

(15)   Godin, M.; Tabard-Cossa, V.; Miyahara, Y.; Monga, T.; Williams, P. J.; Beaulieu, L. Y.; Bruce Lennox, R.; Grutter, P. Cantilever-Based Sensing: The Origin of Surface Stress and Optimization Strategies. *Nanotechnology* **2010**, *21* (7).

(16)   Zhao, Y.; Gosai, A.; Kang, K.; Shrotriya, P. Multiscale Modeling Reveals the Cause of Surface Stress Change on Microcantilevers Due to Alkanethiol SAM Adsorption. *J. Chem. Inf. Model.* **2020**, *60* (6), 2998–3008.

(17)   Vericat, C.; Vela, M. E.; Corthey, G.; Pensa, E.; Cortés, E.; Fonticelli, M. H.; Ibañez, F.; Benitez, G. E.; Carro, P.; Salvarezza, R. C. Self-Assembled Monolayers of Thiolates on Metals: A Review Article on Sulfur-Metal Chemistry and Surface Structures. *RSC Adv.* **2014**, *4* (53), 27730–27754.

(18)   Chen, C. S.; Chou, C. C.; Chang, S. W. Multiscale Analysis of Adsorption-Induced Surface Stress of Alkanethiol on Microcantilever. *J. Phys. D. Appl. Phys.* **2013**, *46* (3).

(19)   Dareing, D. W.; Thundat, T. Simulation of Adsorption-Induced Stress of a Microcantilever Sensor. *J. Appl. Phys.* **2005**, *97* (4).

(20) González, R. I.; Valencia, F. J.; Rogan, J.; Valdivia, J. A.; Sofo, J.; Kiwi, M.; Munoz, F. Bending Energy of 2D Materials: Graphene, MoS2 and Imogolite. *RSC Adv.* **2018**, *8* (9), 4577–4583.

(21) Peng, Z.; Chen, X.; Fan, Y.; Srolovitz, D. J.; Lei, D. Strain Engineering of 2D Semiconductors and Graphene: From Strain Fields to Band-Structure Tuning and Photonic Applications. *Light Sci. Appl.* **2020**, *9* (1).

(22) Martinet, Q.; Baronnier, J.; Girard, A.; Albaret, T.; Saviot, L.; Mermet, A.; Abecassis, B.; Margueritat, J.; Mahler, B. Ligand-Dependent Nano-Mechanical Properties of CdSe Nanoplatelets: Calibrating Nanobalances for Ligand Affinity Monitoring. *Nanoscale* **2021**, *13* (18), 8639–8647.

(23) Deligoz, E.; Colakoglu, K.; Ciftci, Y. Elastic, Electronic, and Lattice Dynamical Properties of CdS, CdSe, and CdTe. *Phys. B Condens. Matter* **2006**, *373* (1), 124–130.

(24) Bouet, C.; Mahler, B.; Nadal, B.; Abecassis, B.; Tessier, M. D.; Ithurria, S.; Xu, X.; Dubertret, B. Two-Dimensional Growth of CdSe Nanocrystals, from Nanoplatelets to Nanosheets. *Chem. Mater.* **2013**, *25* (4), 639–645.

(25) Armon, S.; Efrati, E.; Kupferman, R.; Sharon, E. Geometry and Mechanics in the Opening of Chiral Seed Pods. *Science (80-.).* **2011**, *333*, 1726.

(26) Chu, A.; Livache, C.; Ithurria, S.; Lhuillier, E. Electronic Structure Robustness and Design Rules for 2D Colloidal Heterostructures Electronic Structure Robustness and Design Rules for 2D Colloidal Heterostructures. *J. Appl. Phys.* **2018**, *123*, 035701.

(27) Ithurria, S.; Talapin, D. V. Colloidal Atomic Layer Deposition (c-ALD) Using Self-Limiting Reactions at Nanocrystal Surface Coupled to Phase Transfer between Polar and Nonpolar Media. *J. Am. Chem. Soc.* **2012**, *134* (45), 18585–18590.

(28) Hazarika, A.; Fedin, I.; Hong, L.; Guo, J.; Srivastava, V.; Cho, W.; Coropceanu, I.; Portner, J.; Diroll, B. T.; Philbin, J. P.; Rabani, E.; Klie, R.; Talapin, D. V. Colloidal Atomic Layer Deposition with Stationary Reactant Phases Enables Precise Synthesis of "Digital" II-VI Nano-Heterostructures with Exquisite Control of Confinement and Strain. *J. Am. Chem. Soc.* **2019**, *141* (34), 13487–13496.

(29) Tepliakov, N. V.; Baimuratov, A. S.; Vovk, I. a.; Leonov, M. Y.; Baranov, A. V.; Fedorov, A. V.; Rukhlenko, I. D. Chiral Optical Properties of Tapered Semiconductor Nanoscrolls. *ACS Nano* **2017**, *11* (7), 7508–7515.

(30) Sun, K.; Lee, J.; Xu, C.; Lilly, G. D.; Glotzer, S. C.; Kotov, N. a. Twisted Ribbons. *Science,* **2010**, *1023*, 1355–1359.

(31) Yeom, J.; Yeom, B.; Chan, H.; Smith, K. W.; Dominguez-Medina, S.; Bahng, J. H.; Zhao, G.; Chang, W. S.; Chang, S. J.; Chuvilin, A.; Melnikau, D.; Rogach, A. L.; Zhang, P.; Link, S.; Král, P.; Kotov, N. a. Chiral Templating of Self-Assembling Nanostructures by Circularly Polarized Light. *Nat. Mater.* **2015**, *14* (1), 66–72.

(32) Feng, W.; Kim, J. Y.; Wang, X.; Calcaterra, H. a.; Qu, Z.; Meshi, L.; Kotov, N. a. Assembly of Mesoscale Helices with Near-Unity Enantiomeric Excess and Light-Matter Interactions for Chiral Semiconductors. *Sci. Adv.* **2017**, *3* (3), 1–13.

(33) Zhang, Y.; Zhang, H.; Chen, D.; Sun, C.-J.; Ren, Y.; Jiang, J.; Wang, L.; Li, Z.; Peng, X. Engineering of Exciton Spatial Distribution in CdS Nanoplatelets. *Nano Lett.* **2021**, *21* (12), 5201–5208.

(34)   Timoshenko, B. Y. S. Analysis of Bi-Metal Thermostats. *J. Opt. Soc. Am.* **1925**, *11*, 233–255.

(35)   Huang, M.; Cavallo, F.; Liu, F.; Lagally, M. G. Nanomechanical Architecture of Semiconductor Nanomembranes. *Nanoscale* **2011**, *3* (1), 96–120.

(36)   Neindre, B. L. E. Constantes Mécaniques - Coefficients d'élasticité. *Tech. l'ingénieur* **1991**, *33* (0).

(37)   Rawicz, W.; Olbrich, K. C.; McIntosh, T.; Needham, D.; Evans, E. A. Effect of Chain Length and Unsaturation on Elasticity of Lipid Bilayers. *Biophys. J.* **2000**, *79* (1), 328–339.

(38)   Gupta, R. K.; Suresh, K. A.; Guo, R.; Kumar, S. Langmuir-Blodgett Films of Octadecanethiol - Properties and Potential Applications. *Anal. Chim. Acta* **2006**, *568* (1–2), 109–118.

Table of Contents

RCOO⁻ LIGANDS

$C_nH_{2n+1}S^-$ LIGANDS

Chirality inversion

R

n